

Clinical applications of susceptibility weighted MR imaging of the brain – a pictorial review

Bejoy Thomas · Sivaraman Somasundaram ·
Krishnamoorthy Thamburaj ·
Chandrasekharan Kesavadas · Arun Kumar Gupta ·
Narendra K. Bodhey · Tirur Raman Kapilamoorthy

Received: 25 June 2007 / Accepted: 3 September 2007 / Published online: 11 October 2007
© Springer-Verlag 2007

Abstract

Introduction Susceptibility-weighted imaging (SWI) is a novel magnetic resonance (MR) technique that exploits the magnetic susceptibility differences of various tissues, such as blood, iron and calcification. This pictorial review covers many clinical conditions illustrating its usefulness.

Methods SWI consists of using both magnitude and phase images from a high-resolution, three-dimensional fully velocity-compensated gradient echo sequence. Phase mask is created from the MR phase images, and multiplying these with the magnitude images increase the conspicuity of the smaller veins and other sources of susceptibility effects, which is depicted using minimal intensity projection (minIP).

Results The phase images are useful in differentiating between diamagnetic and paramagnetic susceptibility effects of calcium and blood, respectively. This unique MR sequence will help in detecting occult low flow vascular lesions, calcification and cerebral microbleed in various pathologic conditions and aids in characterizing tumors and degenerative diseases of the brain. This sequence also can be used to visualize normal brain structures with conspicuity.

Conclusion Susceptibility-weighted imaging is useful in differentiating and characterizing diverse brain pathologies.

Keywords Brain · Magnetic resonance imaging · Susceptibility weighted imaging

Introduction

Susceptibility-weighted imaging (SWI) is a novel magnetic resonance (MR) technique that exploits the magnetic susceptibility differences of various tissues, such as blood, iron and calcification [1]. It consists of using both magnitude and phase images from a high-resolution, three-dimensional (3D) fully velocity-compensated gradient echo sequence [2]. Phase mask is created from the MR phase images, and multiplying these with the magnitude images increases the conspicuity of the smaller veins and other sources of susceptibility effects, which is depicted using minimal intensity projection (minIP) [3].

The term susceptibility-weighted imaging has been used by various authors to indicate sequences that are sensitive to T2*gradient echo (GRE) techniques [4]; it has also been referred to as high-resolution (HR) blood oxygen level-dependent (BOLD) venography [1]. However, in this text, we use SWI to refer to the use of magnitude or phase images, or a combination of both, obtained with a 3D, fully velocity-compensated, gradient echo sequence. This 3D SWI can be used to visualize smaller veins and other sources of susceptibility effects, such as hemosiderin, ferritin and calcium.

In this article we highlight the various clinical applications of this relatively new MR technique.

Magnetic resonance imaging acquisition and image processing

Imaging was performed using a 12-channel phased array head coil on a 1.5 T clinical scanner (Avanto- SQ Engine; Siemens, Erlangen, Germany). The SWI sequence parameters were: TR (repetition time), 48 ms; TE (echo time),

B. Thomas (✉) · S. Somasundaram · K. Thamburaj ·
C. Kesavadas · A. K. Gupta · N. K. Bodhey · T. R. Kapilamoorthy
Department of Imaging Sciences and Interventional Radiology,
Sree Chitra Tirunal Institute for Medical Sciences and Technology,
Trivandrum, Kerala 695011, India
e-mail: drbejoy2002@yahoo.com

40 ms; Flip angle, 20°; bandwidth, 80 kHz; slice thickness, 2 mm, with 56 slices in a single slab; matrix size, 512×256. A TE of 40 ms was chosen to avoid phase aliasing, and a flip angle of 20° was used to avoid nulling of the signal from pial veins located within the cerebral spinal fluid (CSF) [3]. The acquisition time was 2.58 min with the use of iPAT factor-2.

The first step was to remove incidental phase variations in the images due to static magnetic field inhomogeneity. We accomplished this by means of a homodyne processing of the phase images, which uses a low spatial frequency phase map generated from the raw data itself. The Hamming-filtered reconstructed phase images were then subtracted from the original phase images using complex division [2, 3, 5]. For paramagnetic substances, the increase in the magnetic field leads to a positive phase (for a left-handed MR system) relative to the surrounding parenchyma and CSF. As a second step, we created the phase mask and carried out unimodal signal processing. The phase mask was then multiplied with the magnitude data to enhance the visualization of vessels or microbleeds [2]. Finally, nine 12-mm thick minIP images were generated; these could be used to demonstrate tortuous structures and show the continuity of veins across slices. The entire image processing was automated and the phase, magnitude and minIP images were available on the main console.

Usefulness of SWI phase imaging

Phase changes induced by different tissues lead to good image contrast in phase imaging. Paramagnetic substances show positive phase shift in left-handed MR systems, such as the Avanto system of Siemens (Erlangen, Germany). Phase information requires no additional scan time but is an inherent part of an MR image. Rauscher et al. found after high pass filtering and phase unwrapping, phase images displayed small anatomic structures that are not easily visible on corresponding magnitude images, such as small veins, deep nuclei with increased iron content or even white matter, with superb contrast and resolution [6].

Calcification can be differentiated from hemorrhage based on differences in susceptibility effects – calcium is diamagnetic and blood products show largely paramagnetic susceptibility [6–9] (Fig. 1). This makes MR comparable to computed tomography (CT) in calcium imaging. However, one has to be very careful in inferring magnetic properties from visual image information since the phase patterns associated with these lesions are not only dependent on the susceptibility difference between tissues but also on the geometry of the lesion [10]. MinIP and filtered phase images of the midbrain (Fig. 2a, b) are able to clearly show mineralization of the red nucleus and the substantia nigra.

Dentate nucleus mineralization is also best visualized in SWI images (Fig. 2c, d). Mineralization, iron and hemorrhage in the basal ganglia are also clearly visualized on phase images (Fig. 2e, f, 14). This may be useful in demonstrating and quantifying mineral deposition in various degenerative brain diseases.

Susceptibility effects due to oxy- and deoxyhemoglobin

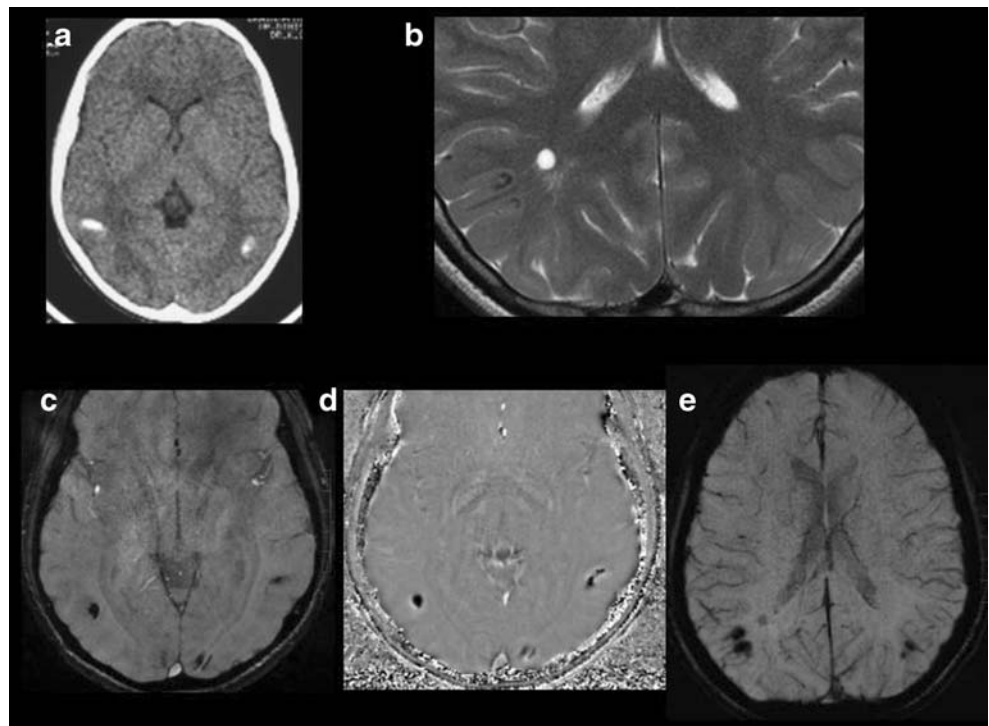
Hemoglobin (Hb) is the primary blood oxygen carrier and is composed of four protein (globin) subunits. Each protein subunit contains a heme molecule that contains an iron atom (Fe^{2+}) surrounded by a porphyrin ring. Oxyhemoglobin is diamagnetic in nature, with no unpaired electrons, and generates magnetic fields that subtract from the external main magnetic field, whereas deoxy-Hb, being paramagnetic with four unpaired electrons, generates magnetic fields that additively combine with the external magnetic field [2]. This property forms the basis for 'BOLD' MR venographic imaging and can also be utilized for imaging the hemoglobin breakdown products.

Susceptibility effects due to non-heme iron and calcium

The major non-heme iron deposition in the human brain is in the form of ferritin [4]. Iron accumulation increases with age and is also observed in various neurodegenerative diseases. Iron is paramagnetic in nature and produces strong susceptibility effects while calcium, being diamagnetic, shows a lower susceptibility effect than iron [7].

Both calcification and iron accumulation in chronic hemorrhage appear as hypointense spots on T2-weighted images and will show a susceptibility effect on T2* imaging. It is not possible to differentiate between these two in conventional MR sequences, and CT is usually required for differentiation. Phase shift of the gradient echo represents an average magnetic field of protons in a voxel, which depends on the susceptibility of this tissues [8]. Yamada et al. showed the phase images to be sensitive to changes in the magnetic field caused by hematoma or calcification and that these differences can be used for differentiating the susceptibility among the tissues [9]. Susceptibility-weighted imaging, with its improved sensitivity in detecting susceptibility effects, can differentiate calcium from hemorrhage and iron deposition with increased sensitivity, as demonstrated in Fig. 1. Calcium is diamagnetic in nature, and the phase shift induced by calcification is opposite to that found with paramagnetic substances like deoxy-Hb, methemoglobin (Met-Hb), hemosiderin and ferritin [7]. Yamada et al. also found all basal ganglia calcifications to exhibit paramagnetic

Fig. 1 Mineralizing microangiopathy in a young male patient. **a** Axial 7-mm-thick non-contrast, enhanced computed tomography (NECT) image showing the calcifications. **b** High-resolution T2 turbo spin echo (TSE) (TR/TE/TA=5260 ms/106 ms/3.42 min, matrix=384×384, nex=4) demonstrating the ‘U’-shaped cortical calcifications in the depth of the sulcus (*arrow*). **c–e** Susceptibility-weighted imaging (SWI) – magnitude, phase and minimal intensity projection (minIP) images, respectively. The lesions are hypointense in all the images, suggesting diamagnetic susceptibility due to calcification (see text). Note also the detailed cerebral venous anatomy visualized in the minIP images (**e**)



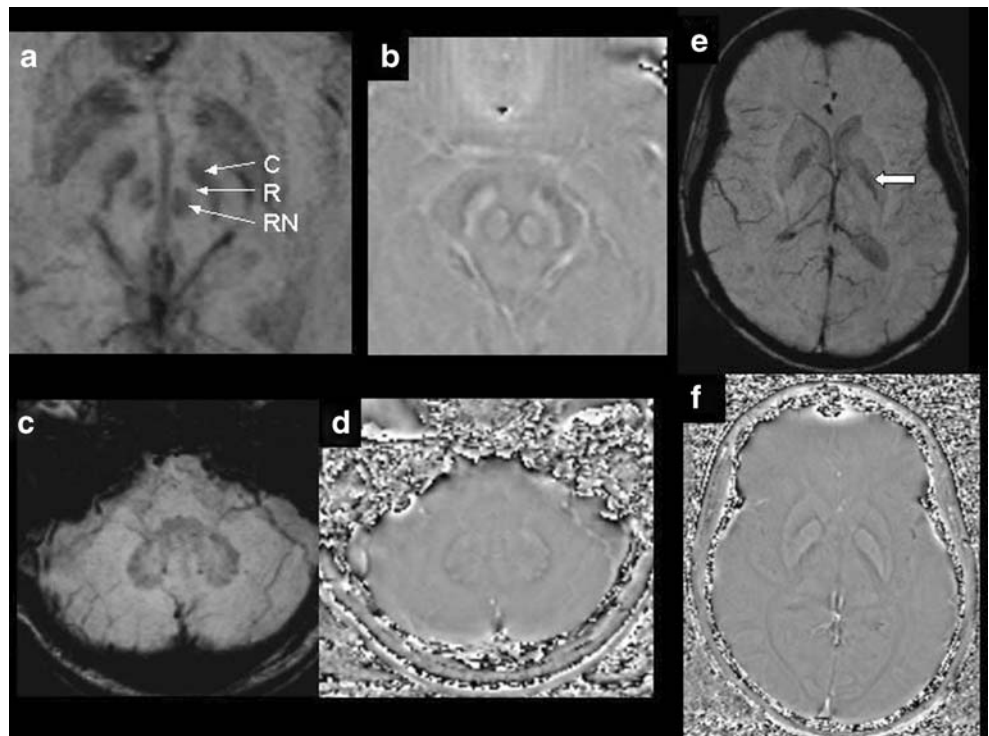
susceptibility and all calcifications outside the basal ganglia to have diamagnetic susceptibility [7]. They proposed that the paramagnetic susceptibility of basal ganglia calcifications might be due to the increased concentration of iron with aging. Gupta et al., in their study of 85 patients with intracranial calcifications and chronic hemorrhages using T2*GRE phase imaging, found the corrected gradient echo

phase images to be useful in differentiating calcifications from chronic hemorrhages [8]

Calcification can be differentiated from the enhancing portions of the granuloma on the phase images (Fig. 3).

However, one should be aware of the possible limitations of this technique in differentiating calcium and blood, as discussed previously.

Fig. 2 **a, b** SWI minIP and phase images, respectively, through the midbrain of a middle-aged adult. Note the mineralization pattern in the red nucleus (RN), pars compacta (C) and reticulata (R) of the substantia nigra. **c, d** Similar sequence through the dentate nucleus of the cerebellum. **e, f** Same sequences at the level of the lentiform nucleus. Note the differential mineralization of the globus pallidus (*thick arrow*)



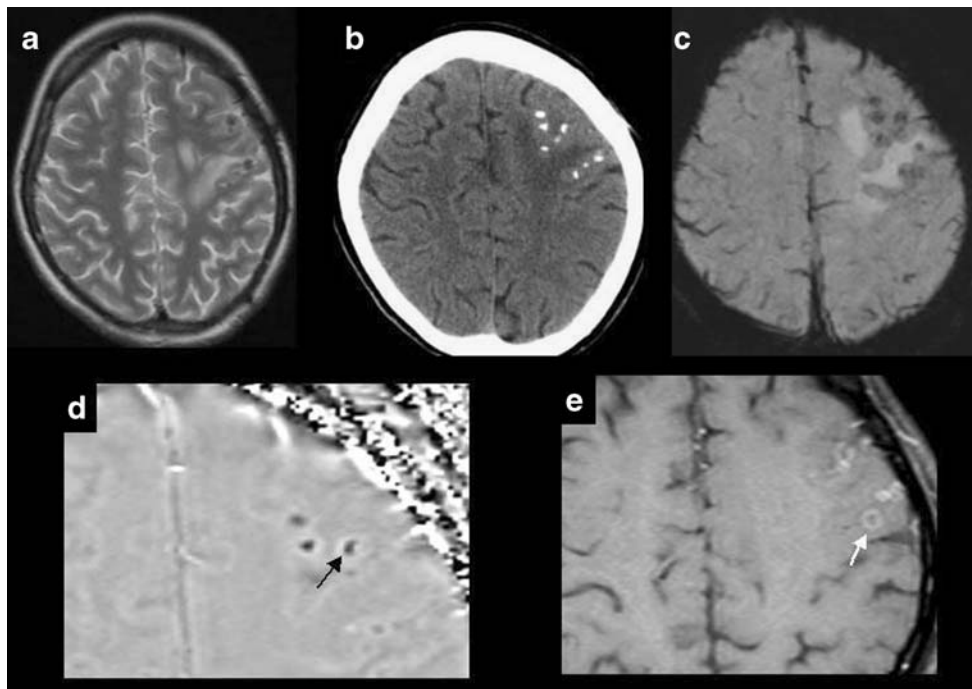


Fig. 3 Calcified granuloma possibly tubercular in origin. **a** T2-weighted axial TSE (TR/ TE/ TA=3010 ms/81 ms/2.29 min, matrix=384×239, nex=1) showing the hypointense lesions in the left frontal lobe with perilesional white matter edema. **b** NECT confirms the presence of calcified lesions with underlying edema. **c** SWI minIP images show the lesions to be hypointense with edema highlighted with a 'FLAIR' (fluid-attenuated inversion-recovery)-like contrast.

d SWI phase images show the central calcified portions of the granuloma with diamagnetic susceptibility (hypointense) and the peripheral ring of hyperintensity (*arrow*), which probably represents paramagnetic deposits in the wall of the active granuloma. **e** Contrast-enhanced (CE) fat-suppressed axial T1-weighted SE (spin-echo) images (TR/TE/TA=776 ms/11 ms/2.05 min, matrix=256×156, nex=1) showing the corresponding rim enhancement (*arrow*)

Blood oxygen level-dependent MR venography/small vessel imaging

The most widely used techniques for MR angiography (MRA) are time of flight (TOF) and phase-contrast MRA [11], with the former being sensitive to rapidly flowing spins and the latter representing the proton velocity map. Time of flight methods use the inflow of fresh unsaturated blood so that the vessels will appear bright compared with the surrounding tissue. They are usually flow compensated, whereas phase contrast methods are velocity-compensated. However, these methods have limitations in terms of their ability to visualize slow flow blood in small vessels.

Susceptibility-weighted imaging uses the paramagnetic deoxy-Hb as an intrinsic contrast agent [1]. Deoxyhemoglobin causes a reduction in T2* as well as a phase difference between the vessel and its surrounding parenchyma [12–14]. The T1 and T2 properties of blood are dependent on the oxygen saturation of the blood, hematocrit and the state of the red blood cells (RBCs) [2]. At 1.5 T, arterial blood has a T2* of approximately 200 ms, while 70% saturated venous blood has T2* of 100 ms. Hence, Long TEs will help in differentiating arteries from veins [15]. When the phase mask is multiplied with the magnitude images, the venous data is enhanced; when veins are not present, there is no change in the signal. The resultant images are displayed using the

Fig. 4 Large developmental venous anomaly of the left cerebral hemisphere. **a** Axial routine gradient echo (GRE) sequence barely shows the abnormality. **b,c** Phase and minIP images of SWI, respectively, demonstrate the lesion well

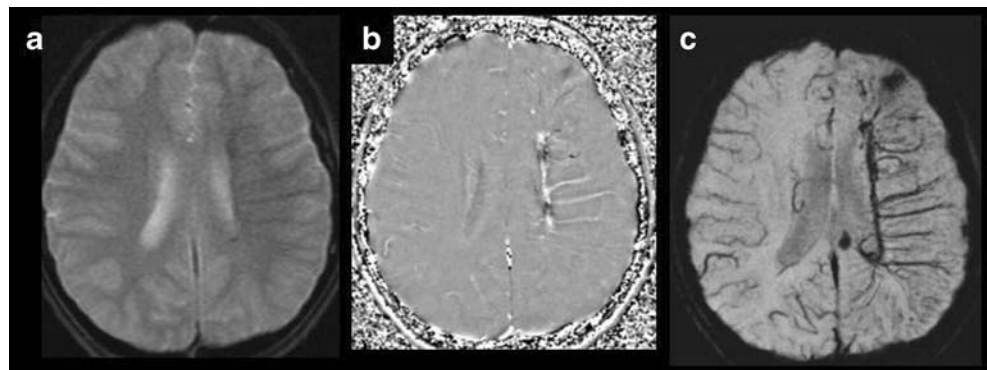
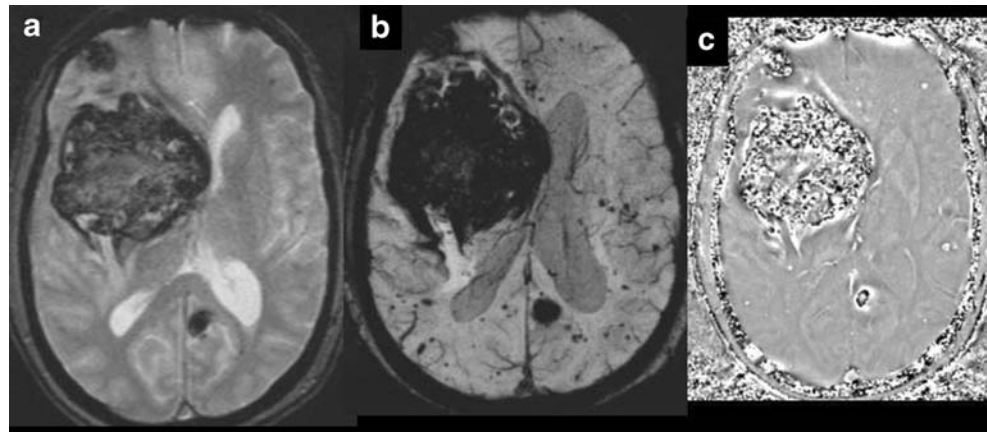


Fig. 5 Multiple cavernomas. **a** Axial routine GRE. **b,c** minIP and phase images of SWI, respectively. Note that the large cavernomas are visualized well by 2D GRE; however, the multitude of smaller ones are detected only by SWI



minimum intensity projection, highlighting the signal from veins and minimizing the signal of adjacent brain tissues [16]. Figures 1e and 2e demonstrate the ability of SWI to depict smaller caliber veins.

Vascular malformations

Developmental venous anomalies (venous angiomas), telangiectasias and cavernomas are low-flow vascular malformations that are less well imaged with conventional MR sequences. Spin-echo sequences are sensitive for imaging high-flow vessels, as evidenced by the flow void phenomenon, but they have reduced sensitivity in imaging small and low flow vessels. Magnetic resonance venography,

such as two dimensional (2D) TOF or phase-contrast MRA, also depicts only large caliber vessels with a poor delineation of slow-flow vessels. The signal intensity of the TOF MRA also diminishes when the direction of blood flow is predominantly within the imaging plane [1]. All of these techniques are sub-optimal for malformed vessels, which exhibit slow multidirectional flow and cause reduced and variable enhancement. Small malformations can be missed entirely due to partial volume effects [1].

While the T2*GRE techniques with small voxel sizes can detect small venous structures, the magnitude and phase information of SWI offers improved sensitivity, revealing low-flow vascular malformations that are invisible on conventional GRE images [1, 17]; this is depicted in Fig. 4. In their study of ten patients, Lee et al. found SWI

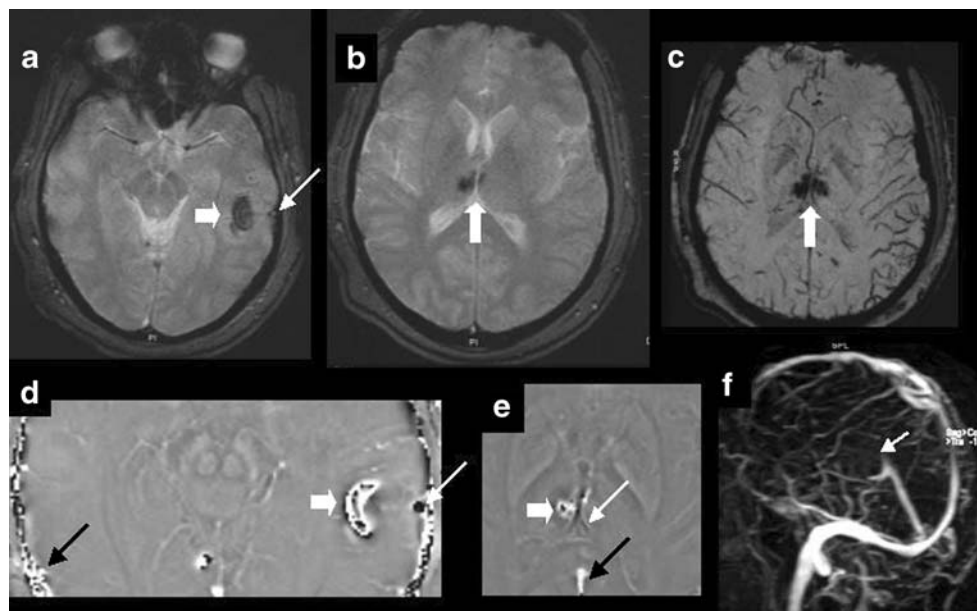
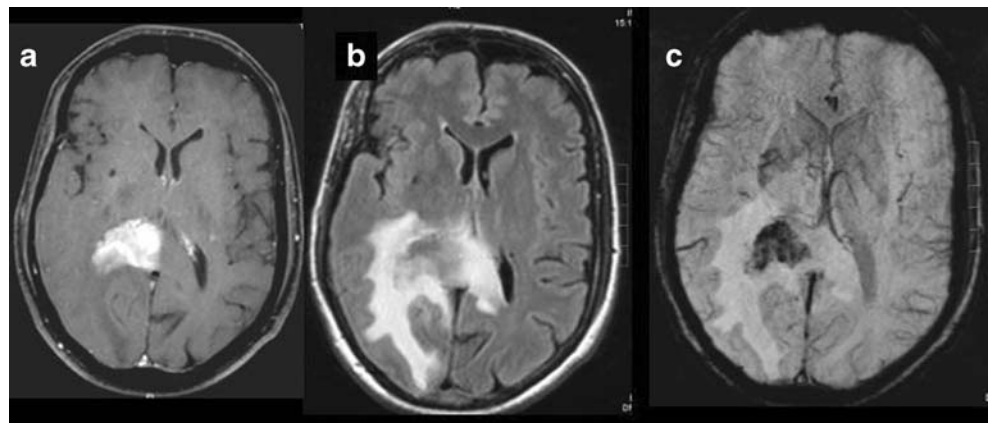


Fig. 6 Venous sinus thrombosis. **a, b** Axial routine 2D GRE. Left temporal and bithalamic hemorrhage (*thick arrows*). Note the prominent left vein of Labbe, which is thrombosed (*thin white arrow*). **c** minIP- SWI showing the bithalamic bleed much more clearly. **d**) Axial phase image at the temporal region showing the thrombosed left vein of Labbe (*thin white arrow*) and the normal right vein of Labbe

(*thin black arrow*) which are in opposite phases. Note also the left temporal hemorrhage (*thick arrow*). **e** Axial phase image at the thalamic level showing the thrombosed internal cerebral veins (*thin white arrow*) and the patent great vein of Galen (*thin black arrow*), which are also in opposite phases. **f** CE MR venography (V) showing the non-opacified internal cerebral veins

Fig. 7 Primary central nervous system (CNS) lymphoma. **a** CE fat-suppressed axial T1-weighted images. Note the intensely enhanced splenial lesion. **b** Axial FLAIR. **c** minIP SWI, showing areas of hemorrhage and perilesional edema well



to be the ideal technique for screening patients with a high clinical suspicion of low-flow vascular malformations [17]. Reichenbach et al. also reported a similar result for developmental venous anomalies [18].

With the help of SWI, more cavernomas are identified that otherwise would not be visualized with conventional T2* techniques, as seen in Fig. 5. The visualization of more lesions may have clinical implications when surgical removal of the lesions for seizure control is being considered. Essig et al. showed SWI to be superior to conventional TOF MR angiography in detecting small arteriovenous malformations [19].

Venous thrombosis

Susceptibility-weighted imaging with both phase and magnitude information facilitates the detection of cortical venous thrombosis which are otherwise difficult to detect in conventional spin-echo T2 images. Lin et al. showed the differentiation of small patent venous structures originating from thrombosis using sequential pre- and post-contrast SWI and the phase pattern in SWI phase images [20]. Figure 6 demonstrates the usefulness of phase images in

identifying thrombosed cerebral veins, especially the cortical veins and those of the deep system.

Brain tumors

Various imaging characteristics that have been suggested to be predictors of glioma grade in humans, including heterogeneity, contrast enhancement, mass effect, cyst formation or necrosis, metabolic activity and cerebral blood volume [21, 22]. In human glioma cells, the levels of ferritin and transferrin receptors detected during immunohistochemical analysis have been shown to correlate with tumor grade [23]. Bagley et al. found T2*-weighted GRE MR images to be valuable in the preoperative grading of gliomas due to the increased susceptibility artifacts caused by hemorrhages [24]. Seghal et al. found SWI to be equivalent to T1 contrast-enhanced (CE) images in the majority of cases studied and, in a few cases, to visualize the lesions better than T1 CE images [25]. These researchers also found an increased sensitivity of non-contrast SWI relative to non-contrast spin echo sequences. Christofridis et al. have observed that the identification of microvasculature in glioblastoma multiforme is facilitated

Fig. 8 Glioblastoma multiforme. **a** CE fat-suppressed axial T1-weighted images showing the necrotic heterogeneously enhancing mass in the right frontal lobe. **b** Axial 2D GRE. **c** minIP SWI. Note that the tumor neovascularity and hemorrhages are better shown in SWI

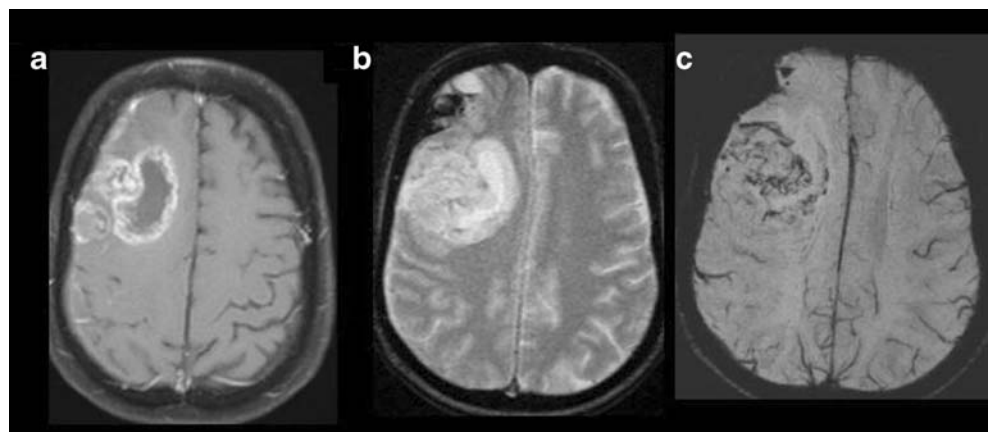
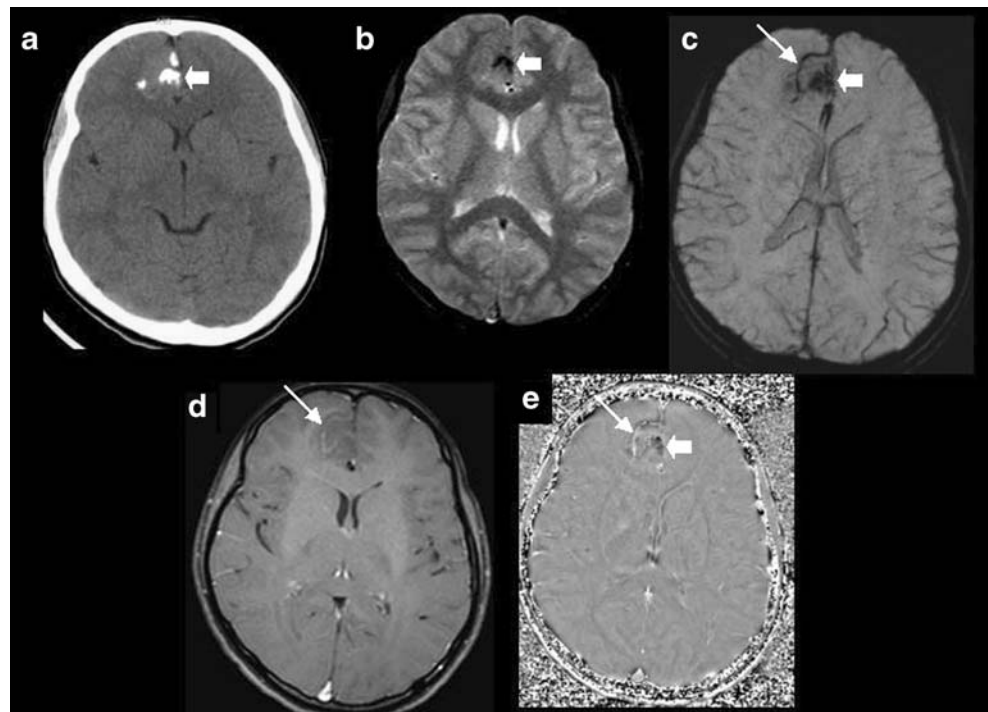


Fig. 9 Right frontal oligodendroglioma. **a** NECT. Note the calcified cortical based lesion (*thick arrow*). **b** Axial 2D GRE showing the calcification (*thick arrow*). **c** SWI minIP showing the calcification (*thick arrow*) and the peripheral vessel (*thin arrow*), both of which are hypointense. **d** CE fat-suppressed axial T1-weighted image showing the enhancing peripheral vein (*thin arrow*). **e** SWI – phase showing the calcification (*thick arrow*) and the deoxy-Hb in the peripheral vein (*thin arrow*) showing opposite phase information; consequently, the two will be differentiated



due to the high resolution on the T2*GRE image in 8T MR [26]. Susceptibility-weighted imaging also provides FLAIR-like contrast because the CSF is suppressed while edema is enhanced relative to the normal tissue [3]. This unique contrast combination of T2* effects and edema within a single image allows for improved detection of space-occupying lesions, as shown in Fig. 7.

Susceptibility-weighted imaging is better able to define the internal architecture of the lesion in comparison to conventional MR sequences as well as to CE T1-weighted images [3]. Figure 8 illustrates the hemoglobin breakdown products within the tumor not detected in conventional images.

Hemorrhage can mimic neoplastic venous vasculature in a tumor due to the similar paramagnetic susceptibility effect

produced by both. However, hemorrhage can be distinguished from veins if SWI is used both before and after the administration of the contrast agent [20]. Blood vessels change their signal intensity, but regions of inactive hemorrhage do not.

Phase images of SWI are needed to differentiate tumor vasculature from calcifications since both show hypointensity on minIP images. Calcium, being diamagnetic, shows negative phase (in left-hand MR systems) and is thereby hypointense in phase images. Tumor vasculature due to the presence of increased deoxy-Hb shows a paramagnetic effect with a resultant positive phase on phase SWI images, as demonstrated in Fig. 9.

Susceptibility-weighted imaging can also differentiate intraaxial tumors from extraaxial tumors by demonstrating the shift of vessels around the mass, as seen in Fig. 10. SWI

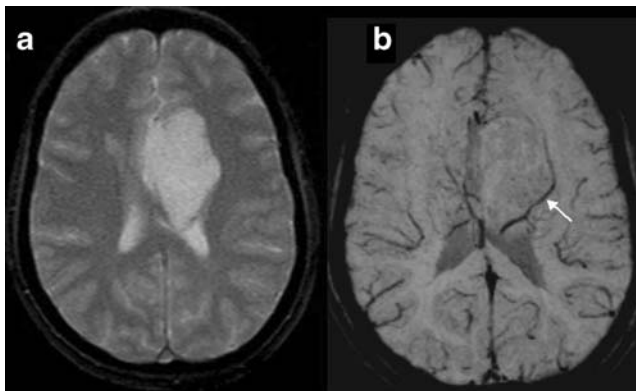


Fig. 10 Interhemispheric epidermoid. **a** Axial 2D GRE, **b** SWI minIP. SWI provides more information as the left thalamostriate and the septal veins (*thin arrow*) are being shifted laterally by the mass

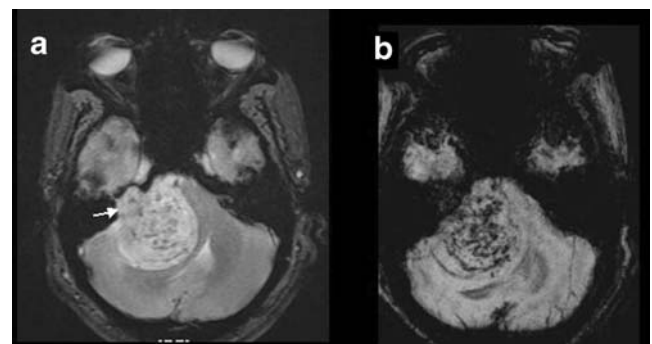
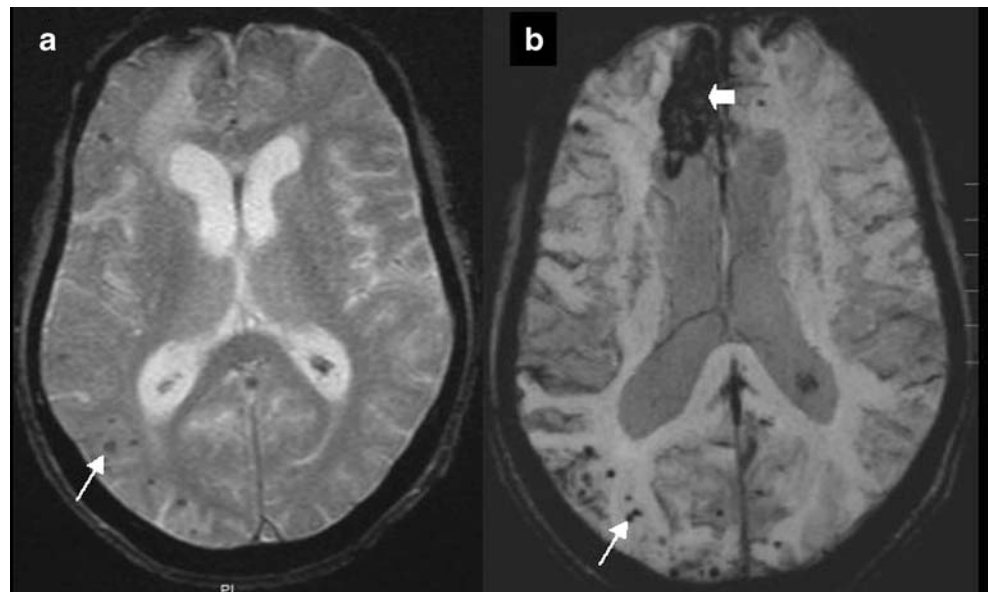


Fig. 11 Right acoustic schwannoma. **a** Axial 2D GRE, **b** SWI minIP. Both show the microhemorrhages within the tumor, but SWI shows them better. Note also the widened right internal auditory meatus (*arrow*)

Fig. 12 Traumatic brain injury **a** Axial 2D GRE, **b** SWI minIP. Multiple microbleeds at the gray-white junction (*arrow*) suggest diffuse axonal injury (DAI). Note also the evidence of right frontal hematoma (*thick arrow*)



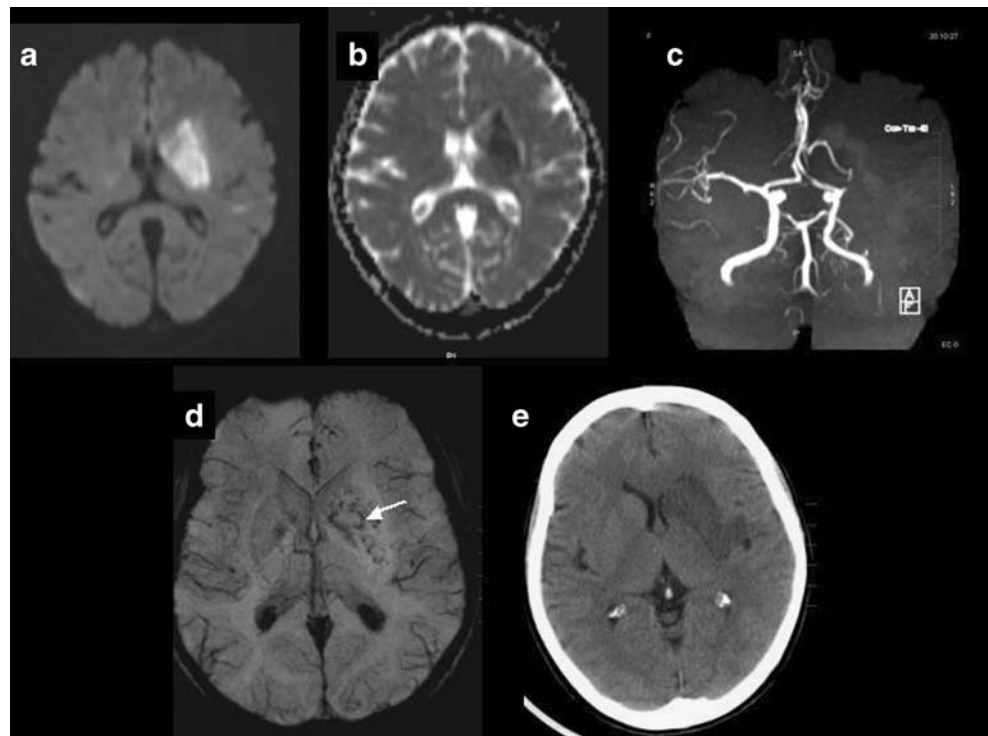
can also be used to differentiate acoustic schwannomas from cerebellopontine angle meningiomas with the improved detection of microhemorrhages within schwannomas, which are not observed in the meningiomas [27] (Fig. 11).

Trauma

About 10% of the CT-proven hematomas show no trace of hemosiderin on routine spin-echo MRI [28]. Diffuse axonal

injury (DAI), a form of traumatic brain injury, is caused by shearing stress, primarily in the white matter [29]. The extent of axonal injury has been correlated with poor outcome [30]. Magnetic resonance imaging is more effective than CT in detecting and classifying injury patterns in DAI when hemorrhagic or non-hemorrhagic [31]. The presence of hemorrhage within the DAI indicates a poor prognosis when compared to lesions without hemorrhage [32]. T2*GRE images enable a better detection of the hemorrhage than conventional MRI techniques [33]. However, recent studies have demonstrated that SWI is

Fig. 13 Left basal ganglia acute infarct. **a** Diffusion-weighted axial image showing the hyperintense acute infarct. **b** ADC map showing restricted diffusion. **c** TOF MRA showing occlusion of the left middle cerebral artery. **d** SWI minIP showing the early detection of microhemorrhages within the infarct (*d, arrow*), which is not shown by a CT taken at the same time (*e*)



more sensitive than GRE imaging for detecting suspected DAI [34]. Figure 12 demonstrates the utility of SWI in detecting punctuate hemorrhages in a patient with a history of trauma and altered sensorium.

Stroke

Acute infarct with or without hemorrhage occurs due to thromboembolism or atherosclerotic stenosis. Susceptibility-weighted imaging is exquisitely sensitive in detecting the presence or absence of hemorrhage within an infarct [35] (Fig. 13). Thromboembolism can also change susceptibility by decreasing arterial flow, thus increasing the amount of deoxy-Hb [36].

The demonstration of bleed within the infarct may influence the subsequent treatment decisions. However, it is not clear at present whether detecting microbleeds within infarcts, which are not picked up by CT, will alter the management.

Cerebral microbleeds (CMB)

Cerebral microbleeds (CMB) are observed in various conditions, such as chronic systemic hypertension [37], cerebral amyloid angiopathy [38], cerebral autosomal dominant arteriopathy with subcortical infarcts and leukoencephalopathy (CADASIL) [39, 40], and in cases of cerebral vasculitis [41]. Computed tomography and conventional MR techniques usually fail to identify the cerebral microbleeds, which are, in contrast, well visualized in gradient T2*-weighted images [42]. Three-dimensional SWI, with its higher sensitivity, identifies numerous microbleeds (Figs. 14, 15) unidentified on routine gradient images.

Lesnik et al. found cerebral microbleeds in 31% of the symptomatic CADASIL mutation carriers, and they also identified that vascular risk factors, such as hypertension, do not account for the microbleeds [39]. Figure 15

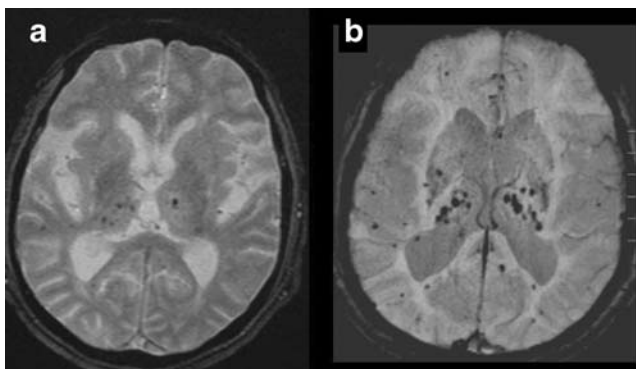


Fig. 14 Hypertensive bleed **a** Axial 2D GRE, **b** SWI minIP. Note the multiple microbleeds at the characteristic locations

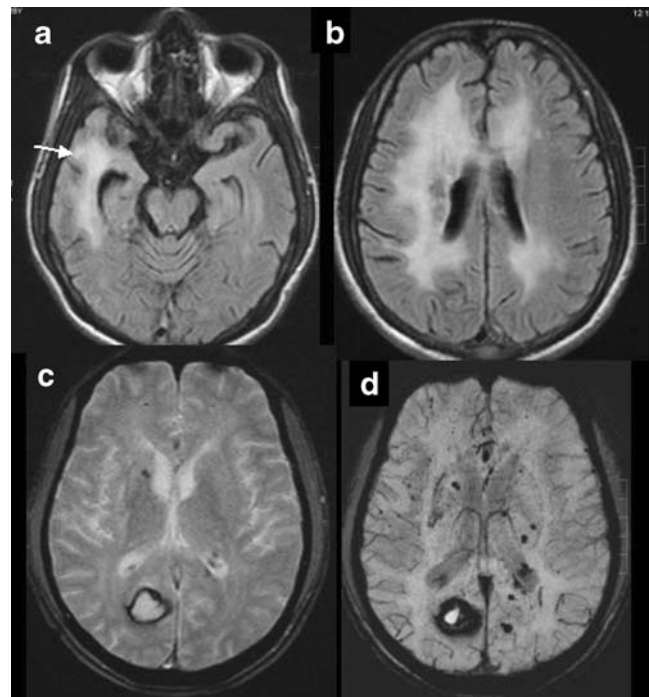


Fig. 15 CADASIL Syndrome. **a, b** Axial FLAIR. Note the extensive white matter hyperintensity, most characteristically visible in the temporal white matter (*arrow*). **c, d** 2D GRE (**c**) and SWI minIP (**d**) showing the distribution of hemorrhages

Martin et al., in their study of 16 symptomatic patients with CADASIL, found a high frequency of microbleeds in CADASIL patients and showed cerebral microbleeds and T2-hyperintense ischemic lesions to be independent manifestations of the underlying angiopathy [40].

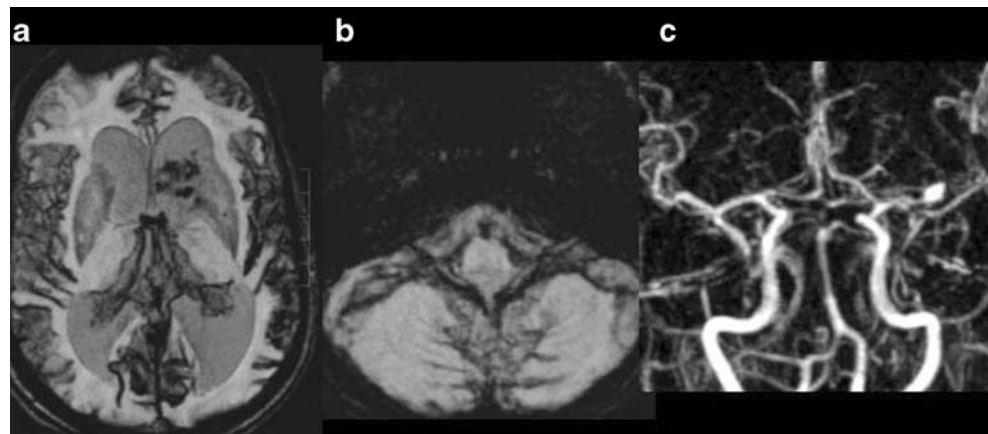
Subarachnoid hemorrhage and pial siderosis

Susceptibility-weighted imaging can demonstrate subacute and chronic subarachnoid hemorrhage, which are usually difficult to be identified with CT and/or conventional MR sequences. Susceptibility-weighted imaging reveals the pial staining of hemosiderin and ferritin in chronic subarachnoid hemorrhage (SAH) not demonstrated even with FLAIR images, as shown in Fig. 16.

Neurodegenerative diseases

Increased iron deposition is found in Parkinson's disease, Huntington's disease, Alzheimer's disease, multiple sclerosis, amyotrophic lateral sclerosis and pantothenate kinase-associated neurodegeneration (PKAN) [43–46]. The capability to measure the amount of non-heme iron in the brain will facilitate a better understanding of the disease progression and will also help in predicting the treatment outcome.

Fig. 16 Subacute subarachnoid hemorrhage. **a, b** SWI minIP showing the extensive susceptibility effects along the subarachnoid spaces and pial siderosis. **c** TOF MRA showing left middle cerebral artery bifurcation aneurysm which had ruptured



Minerals such as calcium (diamagnetic) and iron (paramagnetic) exert different degrees of susceptibility effects, thereby enabling SWI to be a more sensitive means of detecting mineral deposits (Fig. 17). Filtered phase images have been shown to be useful for observing the increased iron content in the brain [47]. However, in any one patient, it will be difficult to differentiate between normal and abnormal mineralization. Haacke et al. recently determined the baseline phase behavior patterns due to mineralization in various brain regions on SWI [48]. Further research is needed to determine its usefulness in differentiating between normal and abnormal mineral deposition in the human brain.

Multiple sclerosis

Multiple sclerosis is usually studied with FLAIR and CE T1 imaging. Susceptibility-weighted imaging can show the perivenular distribution of the demyelinating lesions [49]. Chronic lesions may show evidence of iron deposition within them, which may be better picked up by SWI than by conventional GRE.

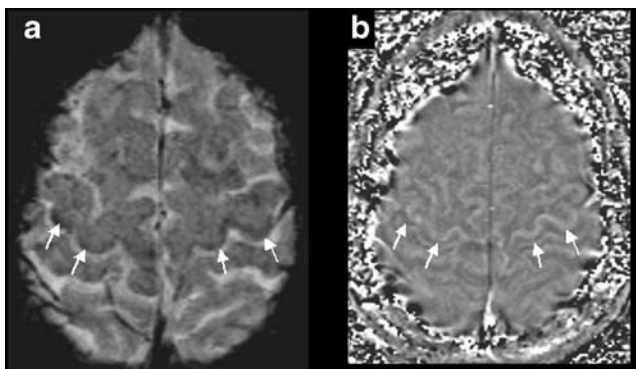


Fig. 17 Degenerative brain disease. SWI minIP (**a**) and phase images (**b**) showing the mineralization along the motor cortex (arrows)

High-resolution MR BOLD venography using T1-reducing contrast agent

Lin et al. [19] found a 26% reduction in data acquisition time while both maintaining the visibility of cerebral venous vessels and reducing the susceptibility artifacts with the use of T1-reducing contrast agent with the SWI. The TE can be reduced from 40 to 25 ms and the TR can be reduced from 57 to 42 ms, thus allowing for an overall time reduction in acquisitions. Reducing the TE minimizes the susceptibility artifacts induced by air-tissue interfaces; this reduction in TR decreases the overall time of acquisition.

High-field SWI

Reichenbach et al. observed an improved resolution and delineation of smaller vessels using high-field 3T MRI instead of low-field MRI [50]. The TE can also be reduced with high field strengths. A higher field strength has the advantage of obtaining images of superior spatial resolution in anatomical venous networks or pathological lesions, such as microbleeds and mineralization, compared to the 1.5T system. However, it is also important to recognize the potential artifacts on SWI at high field strengths due to their higher sensitivity to susceptibility effects. This disadvantage can be offset with optimized protocols; as such, high-field SWI appears to be the future – at least in brain imaging.

Conclusion

Susceptibility-weighted imaging appears to be a promising MR imaging sequence for delineating cerebral microvasculature and detecting foci of micro- and macrohemorrhages and low-flow vascular malformations. It also facilitates the characterization of cerebral tumors and degenerative cerebral

diseases as well as the differentiation between calcification and bleed in the brain.

Acknowledgements We thank Siemens Medical Systems for providing with the SWI sequence and the post-processing tools. We also thank the Director, SCTIMST, for the permission to publish this paper.

Conflict of interest statement We declare that we have no conflict of interest.

References

1. Reichenbach JR, Venkatesan R, Schillinger DJ et al (1997) Small vessels in the human brain. MR venography with deoxyhemoglobin as an intrinsic contrast agent. *Radiology* 204:272–277
2. Reichenbach JR, Haacke EM (2001) High-resolution BOLD venographic imaging: a window into brain function. *NMR Biomed* 14:453–467
3. Seghal V, Delproposito Z, Haacke EM et al (2005) Clinical applications of neuroimaging with susceptibility-weighted imaging. *J Magn Reson Imaging* 22:439–450
4. Liang L, Korogi Y, Sugahara T, Shigematsu Y, Okuda T, Ikushima I, Takahashi M (1999) Detection of intracranial hemorrhage with susceptibility-weighted MR sequences. *AJNR Am J Neuroradiol* 20:1527–1534
5. Wang Y, Yu Y, Li D et al (2000) Artery and vein separation using susceptibility-dependent phase in contrast enhanced MRA. *J Magn Reson Imaging* 12:661–670
6. Rauscher A, Sedlacik J, Barth M, Haacke EM, Reichenbach JR et al (2005) Magnetic susceptibility-weighted MR phase imaging of the human brain. *AJNR Am J Neuroradiol* 26:736–742
7. Yamada N, Imakita S, Sakuma T et al (1996) Intracranial calcification on gradient-echo phase image: Depiction of Diamagnetic susceptibility. *Radiology* 198:171–178
8. Gupta RK, Rao SB, Rajan J et al (2001) Differentiation of calcification from chronic hemorrhage with corrected gradient echo phase imaging. *J Comput Assist Tomogr* 25:698–704
9. Yamada N, Imakita S, Sakuma T et al (1990) Evaluation of the susceptibility effect on the phase images of a simple gradient echo. *Radiology* 175:561–565
10. Deistung A, Mentzel HJ, Rauscher A, Witoszynskij S, Kaiser WA, Reichenbach JR (2006) Demonstration of paramagnetic and diamagnetic cerebral lesions by using susceptibility weighted phase imaging (SWI). *Z Med Phys* 16:261–267
11. Dumoulin CL, Hart HJ (1986) Magnetic resonance angiography. *Radiology* 161:717–720
12. Thulborn KR, Waterton JC, Matthews PM et al (1982) Oxygenation dependence of the transverse relaxation time of water protons in whole blood at high field. *Biochim Biophys Acta* 714:265–270
13. Li D, Waight DJ, Wang Y (1998) In vivo correlation between blood T2* and oxygen saturation. *J Magn Reson Imaging* 8:1236–1239
14. Gomori JM, Grossman RI, Yu-IP C et al (1987) NMR relaxation times of blood: dependence on field strength, oxidation state, and cell integrity. *J Comput Assist Tomogr* 11:684–690
15. Haacke EM, Satin W (1993) Fast imaging and vessel contrast. In: Potchen EJ, Haacke EM, Siebert JE, Gottschalk A (eds) *Magnetic resonance angiography*. Mosby, St. Louis, pp 46–51
16. Reichenbach JR, Venkatesan R, Yablonsky DA et al (1997) Theory and application of static field inhomogeneity effects in gradient echo imaging. *J Magn Reson Imaging* 7:266–279
17. Lee BCP, Vo KD, Kido DK et al (1999) MR high resolution blood oxygenation level dependent venography of occult (low-flow) vascular lesions. *AJNR Am J Neuroradiol* 20:1239–1242
18. Reichenbach JR, Jonetz-Mentzel L, Fitzek C et al (2001) High resolution blood oxygen-level dependent MR venography. *Neuroradiology* 43:364–369
19. Essig M, Reichenbach JR, Schad JR et al (1999) High resolution MR venography of cerebral arteriovenous malformations. *Magn Reson Imaging* 17:1417–1425
20. Lin W, Mukherjee P, An H et al (1999) Improving high resolution MR bold venographic imaging using a T1 reducing contrast agent. *J Magn Reson Imaging* 10:118–123
21. Dean BI, Drayer BP, Bird CR, Flora RA, Hodak JA, Coons SW, Carey RG (1990) Gliomas: classification with MR imaging. *Radiology* 174:411–415
22. Ding B, Ling HW, Chen KM, Jiang H, Zhu YB (2006) Comparison of cerebral blood volume and permeability in preoperative grading of intracranial glioma using CT perfusion imaging. *Neuroradiology* 48:773–781
23. Recht L, Torres CO, Smith TW et al (1990) Transferrin receptor in normal and neoplastic brain tissue: implications for brain tumor immunotherapy. *J Neurosurg* 72:941–945
24. Bagley L, Grossman RI, Judy KD et al (1997) Gliomas: correlation of magnetic susceptibility artifact with histologic grade. *Radiology* 202:511–516
25. Seghal V, Delproposito Z, Haddad D et al (2006) Susceptibility-weighted imaging to visualise blood products and improve tumor contrast in the study of brain masses. *J Magn Reson Imaging* 24:41–51
26. Christoforidis GA, Kangarlu A, Abduljalil AM et al (2004) Susceptibility-based imaging of glioblastoma Microvascularity at 8T.: correlation of MR imaging and postmortem pathology. *AJNR Am J Neuroradiol* 25:756–760
27. Krishnamoorthy T, Radhakrishnan VV, Thomas B et al (2006) Microhemorrhages in vestibular schwannomas: prospective study with T2* weighted gradient-echo sequence. In: *Proc Am Soc Neurorad (ASNR)*. San Diego, USA
28. Wardlaw JM, Statham PF (2000) How often is haemosiderin not visible on routine MRI following traumatic intracerebral haemorrhage? *Neuroradiology* 42:81–84
29. Gentry LR, Godersky JC, Thompson B (1988) MR imaging of head trauma: review of the distribution and radiopathologic features of traumatic lesions. *AJR Am J Roentgenol* 150:663–672
30. Medana IM, Esiri MM (2003) Axonal damage: a key predictor of outcome in human CNS diseases. *Brain* 126:515–530
31. Orrison WW, Gentry LR, Stimac GK et al (1994) Blinded comparison of cranial CT and MR in closed head injury evaluation. *AJNR Am J Neuroradiology* 15:351–356
32. Paterakis K, Karantanas AH, Komnos A et al (2000) Outcome of patients with diffuse axonal injury: the significance and prognostic value of MRI in the acute phase. *J Trauma* 49:1071–1075
33. Atlas SW, Mark AS, Grossman RI et al (1988) Intracranial Hemorrhage: gradient echo MR imaging at 1.5 T.-comparison with spin echo imaging and clinical applications. *Radiology* 168:803–807
34. Tong KA, Ashwal S, Holshouer B et al (2003) Hemorrhagic shearing lesions in children and adolescents with posttraumatic diffuse axonal injury: improved detection and initial results. *Radiology* 227:332–339
35. Wycliffe ND, Chose J, Holshouser B et al (2004) Reliability in detection of hemorrhage in acute stroke by a new three-dimensional gradient recalled echo susceptibility-weighted imaging technique compared to computed tomography: a retrospective study. *J Magn Reson Imaging* 20:372–377
36. Mammen EF (1992) Pathogenesis of venous thrombosis. *Chest* 102:640s–644s
37. Kidwell CS, Saver JL, Villablanca JP et al (2002) Magnetic resonance imaging detection of microbleeds before thrombolysis: an emerging application. *Stroke* 33:95–98

38. Greenberg SM, O'Donnel HC, Schaefer PW et al (1999) MRI detection of new hemorrhages: potential marker of progression in cerebral amyloid angiopathy. *Neurology* 53:1135–1138
39. Lesnik OAJ, Van Den Boom R, Van buchem A et al (2001) Cerebral microbleeds in CADASIL. *Neurology* 57:1066–1070
40. Martin D, Makus H, Jurgen H et al (2002) Cerebral microbleeds in CADASIL: a gradient echo MRI and autopsy study. *Stroke* 33:67–71
41. Campi A, Benndorf G, Filippi M, Reganati P, Martinelli V, Terreni MR (2001) Primary angiitis of the central nervous system: serial MRI of brain and spinal cord. *Neuroradiology* 43:599–607
42. Gernberg SM, Finklestein SP, Schaefer et al (1996) Petechial hemorrhages accompanying lobar hemorrhage: detection by gradient echo MRI. *Neurology* 46:1751–1754
43. Bartzokis G, Tishler TA (2000) MRI evaluation of basal ganglia ferritin iron and neurotoxicity in Alzheimers and huntingtons disease. *Cell Mol Biol* 46:821–833
44. Bartzokis G, Cummins J, Markham Ch et al (1999) MRI evaluation of brain iron in earlier and later onset Parkinsons disease and normal subjects. *Magn Reson Imaging* 17:213–222
45. Hecht MJ, Fellner C, Schmid A, Neundorfer B, Fellner FA (2005) Cortical T2 signal shortening in amyotrophic lateral sclerosis is not due to iron deposits. *Neuroradiology* 47:805–808
46. Vymazal J, Righini A, Brooks RA et al (1999) T1 and T2 in the brain of healthy subjects, patients with Parkinson disease and patients with multiple system atrophy: relation to iron content. *Radiology* 211:489–495
47. Ogg RJ, Langston JW, Haacke EM et al (1999) The correlation between phase shifts in gradient-echo MR images and regional brain iron concentration. *Magn Reson Imaging* 17:1141–1148
48. Haacke EM, Ayaz M, Khan A, Manova ES, Krishnamurthy B, Gollapalli L, Ciulla C, Kim I, Petersen F, Kirsch W (2007) Establishing a baseline phase behavior in magnetic resonance imaging to determine normal vs. abnormal iron content in the brain. *J Magn Reson Imaging* 26:256–264
49. Tan IL, van Schijndel RA, Pouwels PJ, van Walderveen MA, Reichenbach JR, Manoliu RA, Barkhof F (2000) MR venography of multiple sclerosis. *AJNR Am J Neuroradiol* 21:1039–1042
50. Reichenbach JR, Barth M, Haacke M et al (2000) High-resolution MR venography at 3.0 tesla. *J Comput Assist Tomogr* 24:949–957